(Received 22 January 2024, Accepted 25 July 2024, Scheduled 1 September 2024)

Highly Accurate and Efficient 3D Implementations Empowered by Deep Neural Network for 2DLMs-Based Metamaterials

Naixing Feng[1], Huan Wang[1], Xuan Wang[1,*], Yuxian Zhang[1], Chao Qian[2,*], Zhixiang Huang[1], and Hongsheng Chen[2]

[1]*Key Laboratory of Intelligent Computing and Signal Processing, Ministry of Education*
Anhui Laboratory of Information Materials and Intelligent Sensing, Key Laboratory of Electromagnetic Environment Sensing
Anhui Higher Education Institution, Anhui University, Hefei 230601, China
[2]*Interdisciplinary Center for Quantum Information, State Key Laboratory of Modern Optical Instrumentation*
ZJU-Hangzhou Global Science and Technology Innovation Center, College of Information Science and Electronic Engineering
ZJU-UIUC Institute, Zhejiang University, Hangzhou 310027, China

ABSTRACT: Streamlining the on-demand design of metamaterials, both forward and inverse, is highly demanded for unearthing complex light-matter interaction. Deep learning, as a popular data-driven method, has recently found to largely alleviate the time-consuming and experience-orientated features in widely-used numerical simulations. In this work, we propose a convolution-based deep neural network to implement the inverse design and spectral prediction of a broadband absorber, and deep neural network (DNN) not only achieves highly-accurate results based on small data samples, but also converts the one-dimensional (1D) spectral sequence into a 2D picture by employing the Markov transition field method so as to enhance the variability between spectra. From the perspective of a single spectral sample, spectral samples carry not enough information for neural network due to the constraints of the number of sampling points; from the perspective of multiple spectral samples, the gap between different spectral samples is very small, which can hinder the performance of the reverse design framework. Markov transition field method can enhance the performance of the model from those two aspects. The experimental results show that the final value of the soft required accuracy of the one-dimensional fully connected neural network model and the two-dimensional residual neural network model differ by nearly 1%. The final value of the soft accuracy of the one-dimensional residual neural network model is 97.6%, and the final value of the two-dimensional residual neural network model model is 98.5%. The model utilises a data enhancement approach to improve model accuracy and also provides a key reference for designing two-dimensional layered materials (2DLMs) based metamaterials with on-demand properties before they are put into manufacturing.

1. INTRODUCTION

Two-dimensional layer materials (2DLMs), as well known to all, have hitherto become one of the most emerging and popular branches of the material genome. Compared to three-dimensional (3D) materials, outstanding physical properties are discovered and exist in 2DLMs [1]. 2DLMs represent a class of avant-garde nanomaterials, including semi metallic graphene, semiconductor black phosphorus, and insulating hexagonal boron nitride. Each material exhibits unique electronic properties, making it highly favored in the scientific community. In regard to the high-performance separation membranes, 2DLMs with atomic thickness have already played an important and indispensable role for nanostructures [2]. Meanwhile, lattice matching does not need considering in 2DLMs; therefore, different 2DLMs could be applied to different combinations in a whole structure [3–5]. The commonly used 2D materials in the mainstream way are classified as graphene, black phosphorus (BP), transition metal sulfides, and insulators [6]. As a single atomic layer consists of sp2 hybridized carbon, graphene with semimetallic property is first studied in detail [7–9]. So far in the field of photonics, graphene has been known and employed in a wide range of applications due to its strong light-matter interaction and special electrical optics and other properties [10, 11]. Furthermore, it is broadly used in nanophotonic devices, such as modulators [12], plasma-induced transparent devices [13], sensors [14], and photodetectors [15].

To the best of our knowledge, other 2DLMs the same as graphene could also be exfoliated from their parent materials by solution processing, which is a low-cost method for large-scale production [16]. In contrast to graphene, afterward, the monolayer BP with semiconducting property possesses a direct band gap and is more suitable for applications in structures with high on-off ratios [17]. Besides, the monolayer BP could be applied as photodetectors [18], sensors [19], field-effect transistors [20], and solar cells [21]. Moreover, BP similar to other 2DLMs could achieve broadband absorption, ultrafast carrier dynamics, planar properties [22], tunability, and high device performance from mid-infrared to visible wavelengths [23]. As depicted above, both graphene and monolayer BP are widely adopted to design and then fabricate absorbers; however, most of methods are realized based on extensive simulations and continuous trial-and-error approaches, leading to the limit of computational performance and the difficulty in solving local opti-

* Corresponding authors: Xuan Wang (p21201014@stu.ahu.edu.cn); Chao Qian (qianchaozju@zju.edu.cn).

mal solutions. Torun et al. investigated the nature of inter- and intra-layer excitons in transition metal sulfide hetero-bilayers (HBLs) for the benefit of electronic device design and the potential application of these materials in quantum systems [24]. Altıntaş et al. proposed a broadband hypersurface (MS) polarization converter that numerically and experimentally transforms linearly polarized signals into right- or left-handed circularly polarized signals [25]. Abdulkarim et al. developed a novel metamaterial absorber with three-band properties in terahertz band for applications such as imaging and biosensing [26]. Numerical investigation of a multiband perfect metamaterial absorber (MA) based on polarisation-independent cylindrical waveguide has been carried out by Dincer et al. The proposed absorber has a very simple configuration and can operate in a flexible frequency range within the microwave frequency range by simply resizing the structure [27]. Alkurt et al. proposed an antenna-based microwave absorber that absorbs incident waves from different directions, thus providing clearer images during imaging [28]. Valagiannopoulos investigated the arbitrary current distribution on a circular column and how to optimise the radar scattering cross section [29]. Consequently, the urgent task is to find a more efficient and accurate method to significantly reduce the entire cycle time from structural designs, simulation, and analysis, to actual fabrications.

As a branch of the machine learning (ML), deep learning (DL) technique is proposed to enable both rapid design and accurate optimization based on previous datasets and experience [30]. Peurifoy et al. adopted fully connected networks in DL to achieve inverse design and simulated multilayer nanoparticle light scattering [31]. It is demonstrated from experimental results that only small data samples are required to train in the network so that high accuracy could be obtained like traditional simulation methods; besides, the presented method could be several orders of magnitude faster than traditional simulation methods. Furthermore, the framework, proposed by Koziel and Abdullah is based on learning global agent-assisted optimization of the unit cell, local refinement, and maximization of the RCS reduction bandwidth driven directly by electromagnetic (EM) in order to achieve automated and computationally-efficient design of metasurfaces with broadband radar cross-section (RCS) reduction, which could be applied to design the metasurface with its relative bandwidths exceeding 100% [32]. Rodríguez et al. employed an inverse design method in machine learning to create highly optimized 2D plasma metamaterial (PMM) devices [33]. Recently, an inverse-design-based concept was created to construct ultrafast all-optical terahertz (THz) modulators, which inversely designs a THz metasurface supported by electromagnetic induction transparency (EIT) effects by means of the combination of the particle swarm optimization algorithm with the finite-difference time-domain method [34]. Yuan et al. proposed an improved transfer-function-based artificial neural network (ANN) model that could directly generate structural parameters that can match the desired electromagnetic response of the customer [35].

Zhu et al. devised a fast and accurate inverse design method based on migration learning, which was proposed for the design of functional hypersurfaces (hypersurfaces) [36]. Tan et al. explored an innovative approach to develop metamaterials through reverse design techniques to enable optical logic operations on a chip [37]. Tan et al. proposed an electromagnetic correspondence method and demonstrated the ability of the system to solve the equations by decomposing the high-dimensional equations into two low-dimensional matrices [38]. Lee et al. investigated how to implement a complete inverse design of a multilayer filter using a particle swarm optimisation (PSO) algorithm. The results show that the PSO algorithm can be effectively used for the inverse design of multilayer filters, providing a fast and accurate optimisation method [39]. Sheverdin et al. explored how neural networks can be used for the inverse design of photonics, and the proposed method can be generalised to approximate Maxwell interactions [40]. Liu et al. summarised the deep learning approach as a subset of machine learning algorithms that can handle tricky high degree-of-freedom structure design [41]. However, as far as we know, the deep neural network models utilized in previous work have mainly focused on the inverse design of models such as simple multilayer cumulative models or simple strip patterns with single-layer structures, without considering complex multilayer structures with different patterns in different layers. Complex multilayer structures are more difficult to train because of the amount of information to be processed in the neural network.

In this work, we come up with a deep neural network model with both forward prediction and inverse design whose original dataset is derived from a multilayer graphene-BP structure with broadband absorption. Based on small data samples, the proposed DNN model can not only achieve the forward network model in ability of predicting the spectra, but also obtain the inverse design model with capability of predicting structural parameters. To obtain the accuracy of the inverse design network model, we replace traditional numerical methods with forward model surrogate so that the computational time could be greatly saved. Due to the negligible difference in the dataset of 1D absorption spectral sequences, which would affect the training result of model, finally we employ the Markov transfer field approach to convert 1D sequences into 2D pictures for achieving the effect of data enhancement. Our work greatly reduces the heavy dependency on the quality of training data and enhances the data sensitivity in spectral sequences.

2. STRUCTURE AND METHODOLOGY

2.1. Structure Composition

The basic unit of the constructed absorber consists of a bilayer structure with three layers of graphene-BP mixture, which has a single layer of graphene in the upper layer and a monolayer of BP in the bottom layer. The overall structure is shown in the middle large figure in Fig. 1, and the attached drawings on both sides are the top and bottom views of each layer of the structure. In this structure, the insulating layer is made of SiO_2, which is applied to separate the monolayer graphene from the monolayer BP. The purpose of the insulating layer is to block charge carrier transport between the graphene and monolayer BP and to keep its high charge carrier mobility. The first layer of the structure consists of a rectangle with length and width a_1

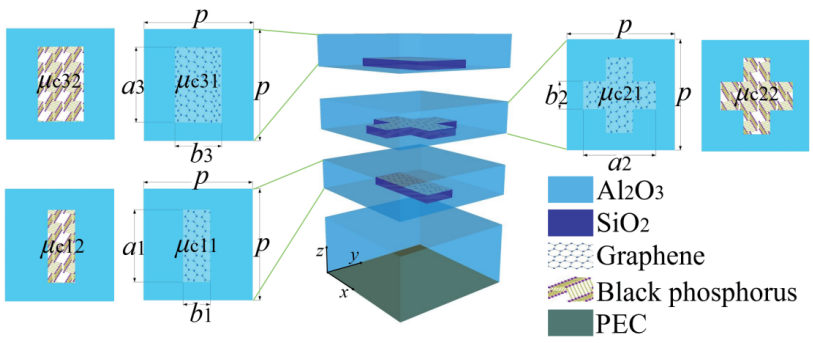

FIGURE 1. Schematic diagram of the three-layer structure of the graphene-black phosphorus hybrid.

and b_1, respectively; the second layer consists of two identical rectangles stacked vertically with length and width a_2 and b_2, respectively; the third layer is similar to the first layer and is a rectangle with length and width a_3 and b_3, respectively. The unit cycle length of the structure is p; the thickness of the dielectric layer is d_1; the thickness of the insulating layer is d_2; the spacing of the layers is d_3; the Fermi energy levels of the first layer of graphene and black phosphorus are μ_{c11} and μ_{c12}. The Fermi energy levels of the second layer of graphene and black phosphorus are μ_{c21}, μ_{c22}. The Fermi levels of the third layer of graphene and black phosphorus are μ_{c31}, μ_{c32}. The three-layer structure formed by the simultaneous combination is encapsulated in aluminum oxide (Al_2O_3) and deposited on an Al_2O_3 substrate. The dielectric constants of the SiO_2 and Al_2O_3 used were 3.9 [42] and 3.2 [43], respectively. Throughout the experiments, the incident light was directed downward perpendicular to the top direction. Moreover, during the calculation, we apply the equations of surface conductivity of graphene and black phosphorus to calculate the corresponding electric field components.

The surface conductivity of graphene is expressed through the Kubo equation as [44]

$$\sigma(\omega,\mu_C,\Gamma,\mathrm{T}) = \sigma_{intra} + \sigma_{inter} \tag{1}$$

$$\sigma_{intra} = \frac{je^2\mu_C}{\pi\hbar^2(\omega - j2\Gamma)}\int_0^{\infty} \left[\frac{\partial f_d(\xi,\mu_C,\mathrm{T})}{\partial\xi} - \frac{\partial f_d(-\xi,\mu_C,\mathrm{T})}{\partial\xi}\right] d\xi \tag{2}$$

$$\sigma_{inter} = -\frac{je^2(\omega - j2\Gamma)}{\pi\hbar^2}\int_0^{\infty} \frac{\partial f_d(-\xi,\mu_C,\mathrm{T}) - \partial f_d(\xi,\mu_C,\mathrm{T})}{(\omega - j2\Gamma)^2 - 4(\xi/\hbar^2)^2} d\xi \tag{3}$$

$$f_d(\xi,\mu_C,\mathrm{T}) = \left(e^{(\xi-\mu_C)/k_B\mathrm{T}} + 1\right)^{-1} \tag{4}$$

where σ_{intra} is the in-band carrier electron component of the surface conductivity, and σ_{inter} is the inter-band carrier electron component of the surface conductivity. $f_d(\xi, \mu_c, T)$ is the Fermi-Dirac distribution. Γ denotes the scattering rate and can be expressed as $\Gamma = 1/(2\tau)$, $\tau = 1\,\mathrm{ps}$. In the finite element method (FEM) calculations, when the ambient temperature is set to 300 K, compared to the in-band contribution conductivity, the surface interband conductivity in the conductivity is too small to be neglected. Therefore, the graphene conductivity at this time can be simplified as

$$\sigma \approx \sigma_{intra} = -\frac{je^2\mu_C}{\pi\hbar^2(\omega - j2\Gamma)} \tag{5}$$

The surface conductivity equation for a single-layer BP using the semi-classical Drude model is given by the following equation [45]

$$\sigma_x = \frac{jD_x}{\pi(\omega + j\eta/\hbar)} \tag{6}$$

$$\sigma_y = \frac{jD_y}{\pi(\omega + j\eta/\hbar)} \tag{7}$$

$$D_j = \frac{\pi e^2 n_s}{m_j}(j = x, y) \tag{8}$$

Here, σ_x and σ_y denote the surface conductivity in the x and y directions. D_x and D_y denote the weight of Drude in the x and y directions, respectively, depending on the effective electron mass m_j in the x or y direction. η denotes the relaxation rate set to 10 meV, which determines the relaxation rate of BP. n_s denotes the doping level of electrons and is set to $2\times10^{13}\,\mathrm{cm}^{-2}$. The electron mass in the x or y direction can be calculated by the following equation:

$$m_x = \frac{\hbar^2}{\frac{2\gamma^2}{\Delta} + \eta_C} \tag{9}$$

$$m_y = \frac{\hbar^2}{2\nu_C} \tag{10}$$

where $\gamma = \frac{4a}{\pi}\,\mathrm{eVm}$, $\Delta = 2\,\mathrm{eV}$, $\eta_C = \frac{\hbar^2}{0.4m_0}$, $\nu_C = \frac{\hbar^2}{1.4m_0}$, $a = 2.23\times10^{-10}\,\mathrm{m}$.

2.2. Dataset Composition

We select two kinds of parameters in the structure. One is the structural parameters a_1, b_1, a_3, and b_3 of the structure, and the other is the Fermi energy levels of the two materials μ_{c11}, μ_{c12}, μ_{c21}, μ_{c22}, μ_{c31}, and μ_{c32}. These 10 parameters are collectively referred to as the structural parameters. The structure parameters are set randomly, and the corresponding spectra of the structure are obtained by employing the FEM method to produce the data set. The spectra are located in the $5 \sim 40\,\mu\text{m}$ wavelength band with 351 sampling points. Eventually, the training set contains 50120 samples, and the test set contains 1000 samples. The test set and training set data are independent without duplicate data. The one-dimensional spectral sequence is then transformed into a two-dimensional image by Markov transition field method, and the image is normalized by the mean and variance of the image.

In the forward prediction, we consider to use 10 structural parameters as input and the spectrum corresponding to each parameter as its label.

In the inverse design, we take the absorption spectra as input and the structural parameters of each spectrum as its label.

2.3. One-dimensional Sequence to Two-Dimensional Picture Conversion Method

There are two conventional methods to solve the problem of too small training data set. One is to use the data augmentation method, and the other is to use transfer learning. However, the performance of transfer learning cannot be guaranteed. Sometimes, the performance even becomes worse than that without transfer learning. In other word, transfer learning is like a 'black box' without revealing its internal mechanism, which heavily relies on the brute-force attack of features and lacks reasonable explanation, so we choose the data augmentation method to optimize the network. By data augmentation, we mean changing the input data without changing the output label values. We apply the Markov translation field (MTF) method to transform a one-dimensional sequence into a two-dimensional picture [46]. In this process, we do not change the output labels, but transform the input data. The connection between the values before and after the sample is strengthened by MTF, because MTF is a method for converting temporal data into spatial data.

First, given a one-dimensional sequence $X = \{x_1, x_2, \ldots, x_n\}$, it is divided into Q quantile bins according to its defined domain range, and each element x_i ($i \in [1, n]$) in the sequence is assigned a unique quantile bin q_j ($j \in [1, Q]$) corresponding to it. Second, a Markov transfer matrix W of order $Q \times Q$ is constructed. Elements $\omega_{i,j}$ in matrix W are given by the frequency of a point in the quantile box q_i followed by a point in the quantile box q_j and normalized to $\omega_{i,j}$. It represents the transfer probability from state i to state j. However, the Markov transfer matrix W is insensitive to the original sequence distribution, which can lead to excessive information loss in the data during the transition. Therefore, it is necessary to define the Markov transition domain:

$$M = \begin{bmatrix} \omega_{ij|x_1 \in q_i, x_1 \in q_j} & \cdots & \omega_{ij|x_1 \in q_i, x_n \in q_j} \\ \omega_{ij|x_2 \in q_i, x_1 \in q_j} & & \omega_{ij|x_2 \in q_i, x_n \in q_j} \\ \vdots & \ddots & \vdots \\ \omega_{ij|x_n \in q_i, x_1 \in q_j} & \cdots & \omega_{ij|x_n \in q_i, x_n \in q_j} \end{bmatrix} \tag{11}$$

where M_{ij} denotes the probability of transfer from the quantile box q_i of x_i to the quantile box q_j of x_j, i.e., the matrix W containing the transfer probabilities on the magnitude axis is expanded into the MTF matrix by considering each sequential point position. For example, $M_{i,j||i-j|=k}$ denotes the transfer probability for a time interval of k points, and then M_{ii} of the main diagonal denotes the self-transfer probability of each quantile box.

2.4. Deep Neural Network Models

Small data sets are prone to problems such as outliers that are difficult to avoid and models that are difficult to optimize. For this data set, the first four structural labels have a large number of values over 100, while the last six Fermi energy level labels are values not exceeding 1. Therefore, the first four values become large outliers. So, we add the normalization process in the model, which is helpful to improve the stability of the model and obtain a more reasonable model. Second, simple small models should be used for training small data sets. Selecting a small and simple model can limit some complex assumptions, reduce the search space of the model, make the model more stable and easier to optimize.

2.4.1. Proxy Model

The solution space in inverse design is non-convex, which will consume much time. Therefore, we use a proxy net to obtain the predicted spectra instead of applying the FEM method, which can greatly save time and cost. The overall model framework and proxy network are reflected in Fig. 2. If the real spectra are directly compared with the predicted spectra of the structural parameters obtained by the proxy net, the accuracy of the proxy net has an upper limit, so the accuracy obtained by the comparison will be biased. Therefore, to reduce the bias brought by the proxy net, we also input the real parameters into the proxy net, so that we can obtain the spectra of the predicted parameters and the spectra of the real parameters at the same time, and then compare these two spectra to obtain the accuracy of the inverse model.

2.4.2. Forward Model

In the forward and inverse deep neural network models, the learning rate, optimizer, and loss function are the same. First, adaptive learning rates are applied in both models, and the learning rate decay function is a cosine annealing schedule table. The learning rate decreases slowly with training, then accelerates, and finally reduces to zero. Second, the optimizer of the model is a stochastic gradient descent (SGD) optimizer, which does not need to calculate the gradient of all samples,

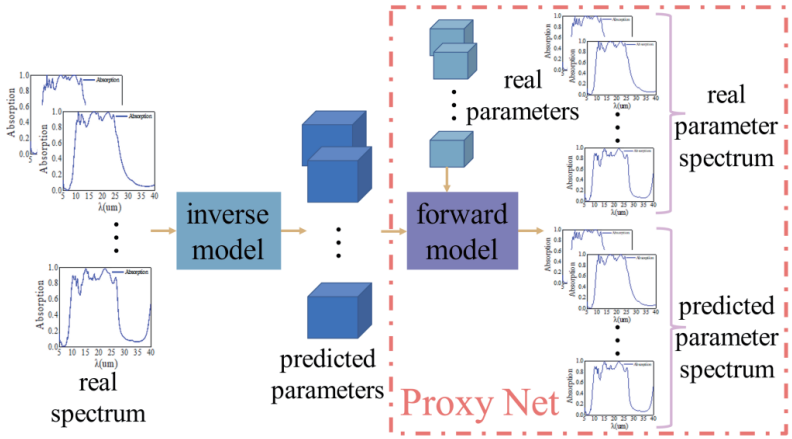

FIGURE 2. The overall model framework contains the agent model. Where dark blue is the predicted structural parameters and light blue is real structural parameters. The horizontal coordinate in the absorption spectrum plot is the wavelength and the vertical coordinate is the absorbance.

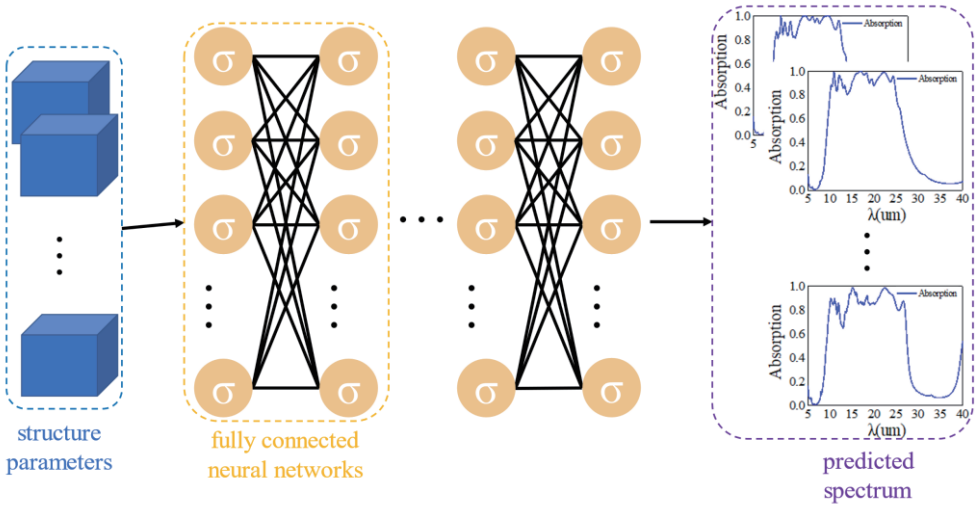

FIGURE 3. Forward deep neural network model. The blue squares represent the structural parameters with 600 neurons per fully connected layer, and each fully connected layer is followed by a BN layer and the Relu activation function.

and it is fast, simple, and efficient to implement. Third, the loss function in the deep neural network model uses the mean squared error loss function (MSE). The function image curve of MSE is smooth, continuous, and derivable everywhere on the curve, which is convenient for using the gradient descent method.

In terms of the specific network model, the forward model differs from the inverse model. The forward model is based on an eight-layer fully connected network with 600 neurons in each layer, and each fully connected layer is followed by a Batch Normalization (BN) layer and a Relu activation function, as seen in Fig. 3. The BN layer can enable the inputs of each layer of the deep neural network in the model to be forced to a standard normal distribution with mean zero and variance one, so that the inputs can remain homogeneously distributed, which will greatly accelerate the training speed. Because the parameters need to be updated after each layer of deep neural network, the distribution of the input data of the previous layer of deep neural network is changed. When the number of layers of the deep neural network increases, the deviation of the distribution of the input data will gradually accumulate; the model training will become more and more complicated; and the model convergence will become slower and slower. Firstly, the BN layer can control the gradient explosion and prevent the gradient from disappearing. With BN layer, the output of the network will not be too large, so a large gradient can be obtained, which avoids a gradient disappearance and then speeds up the convergence of the learning rate. Compared with other activation functions, like a sigmoid function, the simple computation of Relu activation function can greatly reduce the computational effort and improve the computational efficiency. Secondly, the Relu activation function will make part of the output become zero, which could enhance the sparsity of the network, reduce the interaction between parameters, and hence help to alleviate the overfitting phenomenon.

The forward model needs to discriminate its similarity with the real spectrum after training, so three kinds of similarity discriminating parameters are added, including cosine similarity,

Pearson correlation coefficient, and Kendall correlation coefficient. First, cosine similarity, also known as cosine similarity, is adopted to measure the similarity between two vectors. It is measured by calculating the cosine of the angle between the two vectors. In the specific model, we make vectors of each sampled point with respect to the origin so that the sampled point vector in the predicted spectrum is compared with the sampled point vector in the original target spectrum. If the cosine value between them is larger, close to 1, the smaller the angle between the vectors is, close to 0, indicating that the two vectors are more similar; conversely, if the cosine value between them is smaller, close to 0, the larger the angle between the vectors is, close to 90°, indicating that the two vectors are less similar. Second, the Pearson correlation coefficient is also known as the Pearson product moment correlation coefficient [47]. The Pearson correlation coefficient is a linear correlation coefficient used to measure the correlation between variables X and Y. Its value is between -1 and 1, and the larger the value is, the stronger the correlation is between the two variables. When the value of Pearson's correlation coefficient is less than 0, that is, in the range of -1 to 0, the two variables are negatively correlated, that is, when the value of X is larger, the value of Y is smaller; when the value of Pearson's correlation coefficient is greater than 0 and less than 0.3, the two variables are not negatively correlated, but very weakly correlated, and the two variables are basically uncorrelated or uncorrelated. When the value of Pearson's correlation coefficient is greater than 0.3 and less than 0.5, the two variables are slightly correlated. When the value of Pearson's correlation coefficient is greater than 0.5 and less than 0.8, the two variables are moderately correlated, where the interval greater than 0.6 can also be called strong correlation. When the value of Pearson's correlation coefficient is greater than 0.8 and less than 1, the two variables are very strongly correlated. The specific Pearson correlation coefficient calculation formula is shown below

$$r = \frac{\sum_{i=1}^{n} (x_i - \bar{x})(y_i - \bar{y})}{\sqrt{\left[\sum_{i=1}^{n} (x_i - \bar{x})^2\right]\left[\sum_{i=1}^{n} (y_i - \bar{y})^2\right]}} \tag{12}$$

where r denotes the Pearson correlation coefficient; n denotes the variable X and variable Y containing n elements; $\bar{x}$ is the mean of variable X; and $\bar{y}$ is the mean of variable Y.

Third, the Kendall correlation coefficient is similar to the Pearson correlation coefficient and belongs to one of the three major statistical correlation coefficients [48]. The Kendall correlation coefficient, also known as the Kendall rank correlation coefficient, is a statistic used to measure the correlation of two random variables and takes values between -1 and 1. The Kendall correlation coefficient is discriminated in the same way as the Pearson correlation coefficient. There are two formulas for calculating the Kendall correlation coefficient. One is τ_a, and the other is τ_b. The exact form is shown below

$$\tau_a = \frac{c - d}{\frac{1}{2} n (n-1)} \tag{13}$$

$$\tau_b = \frac{c - d}{\sqrt{(c + d + t_x)(c + d + t_y)}} \tag{14}$$

where n denotes the number of samples, so there are $1/2{*}n(n-1)$ combinations; c denotes the number of combinations of elements in two variables X and Y that have consistency (two elements as a pair); d denotes the number of combinations of elements in two variables X and Y that have inconsistency, i.e., divergent elements; t_x and t_y denote the number of tied ranks in variable X and the number of tied ranks in variable Y.

2.4.3. Inverse Model

The depth of the network is crucial to the training of the model. Theoretically, when the depth of the model is increased, better training results can be obtained. However, in the actual training process, as the depth of the model increases, the training results become worse instead; the accuracy decreases; and the model appears to degrade the problem in terms of network structure. In the extreme case, when we superimpose a new layer on the shallow deep neural network, the new layer does not learn new knowledge, but just makes a constant mapping with the shallow layer; the training result of deep neural network should be at least consistent with the shallow model; no degradation should appear; and the degradation phenomenon is not related to overfitting. Ultimately, it is the method of training that is problematic, and the model is not easily optimized. Therefore, we used a residual structure in the inverse design [49]. The residual learning framework was proposed by He et al. to solve the model degradation problem. Let the input be x, and its corresponding underlying mapping is noted as $H(x)$. The next suitable mapping for another stacked nonlinear layer is also the residual $F(x)$, which has the value of $H(x) - x$. Thus, the original underlying mapping $H(x)$ becomes $F(x) + x$. Even if the residual is zero, the output of the stacked layer is at least the original input, which is equivalent to the network doing a constant mapping.

The inverse model specifically uses a resnet18 network. The specific network architecture of the inverse design model is illustrated in Fig. 4, and the number of building blocks and stacking blocks is seen in Table 1. From Fig. 5 and Table 1, it is clear

TABLE 1. Resnet18 network architecture.

Layer name	Output size	18-layer
input_stem	112×112	7×7, 64, stride 2
		3×3 max pool, stride 2
Stage 1	56×56	$\begin{bmatrix} 3 \times 3 & 64 \\ 3 \times 3 & 64 \end{bmatrix} \times 2$
Stage 2	28×28	$\begin{bmatrix} 3 \times 3 & 128 \\ 3 \times 3 & 128 \end{bmatrix} \times 2$
Stage 3	14×14	$\begin{bmatrix} 3 \times 3 & 256 \\ 3 \times 3 & 256 \end{bmatrix} \times 2$
Stage 4	7×7	$\begin{bmatrix} 3 \times 3 & 512 \\ 3 \times 3 & 512 \end{bmatrix} \times 2$
	1×1	Average pool, 10-d fc
FLOPs		1.8×10^9

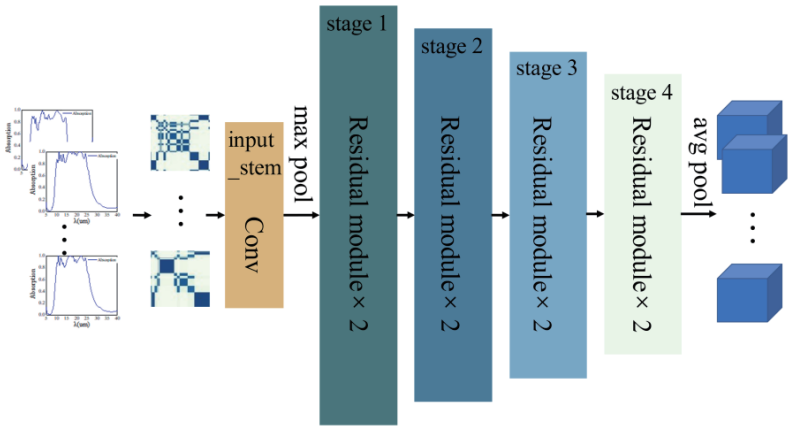

FIGURE 4. Diagram of the resnet18 network architecture model. Where the blue squares represent the structure parameters.

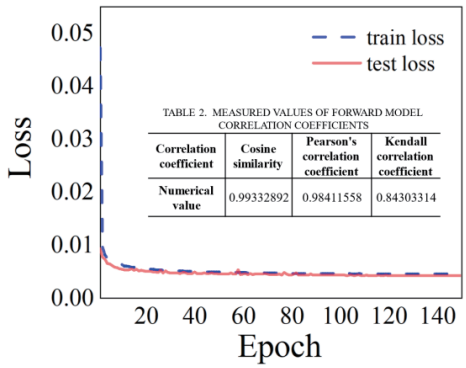

TABLE 2. MEASURED VALUES OF FORWARD MODEL CORRELATION COEFFICIENTS

Correlation coefficient	Cosine similarity	Pearson's correlation coefficient	Kendall correlation coefficient
Numerical value	0.99332892	0.98411558	0.84303314

FIGURE 5. Training loss as well as testing loss of the forward model.

that the network structure contains mainly an input_stem and 4 building stages. Input_stem contains a convolutional layer with a convolutional kernel of $7 * 7$, channel 64, and step 2. Each of the 4 building stages contains 2 residual blocks, and only the first convolutional step in the first residual block is 2, using the following sampling. In this way, it gets smaller and smaller in size and larger in number of channels through 4 building stages.

3. RESULTS AND DISCUSSION

3.1. Forward Model Training Results

Before training the inverse model one has to train the forward model so that the trained forward model can act as a proxy model. We set 150 epochs for the forward model. We also set the batch size to 256, use the learning rate decay method of the cosine annealing schedule, and set the initial learning rate to 0.1. As can be seen in Fig. 5, for the training loss, the training loss of the forward model is reduced to 0.005 at 32 epochs and at 102 epochs. Although the minimum value of the training loss is 0.0044 at 102 epoch, there are still fluctuations in the training loss at this time. After 109 epochs, the training loss of the forward model is stable at 0.0044. The initial value of the test loss is significantly smaller than the training loss, 0.0092, and the test loss can be reduced to 0.005 at epoch 17. For the evaluation of the forward model, we used three correlation coefficients containing cosine similarity, Pearson's correlation coefficient, and Kendall's correlation coefficient, and their corresponding measurements are concluded in Table 2. We could clearly see that the values of the three correlation coefficients are in the interval of extremely strong correlation, which indicates that our spectra obtained by the forward model are extremely well correlated with the real spectra, and the forward model is valid.

3.2. Comparison of Inverse Design Results

In the inverse model, we convert the one-dimensional training data into a two-dimensional image by the MTF method, and the spectrum before conversion is plotted in Figs. 6(a) and (b) against the two-dimensional image after conversion. The spectrum before conversion corresponds to a one-dimensional sequence. The converted two-dimensional image is a symmetric graph about the main diagonal, meaning that any difference in the lower-left region is mirrored in the upper-right region, effectively amplifying the differences between spectral data points and is beneficial to the training of the inverse model. We have small connections between sample points during spectral sampling, but at the same time the MTF method is a time-series image coding method that strengthens the connections between sample sampling points when being used.

The decay curve of the resnet18 network model trained on 2D images is shown in Fig. 6(c). The initial learning rate of the inverse model at this point is 0.1. After using the cosine annealing method, the learning rate decays slowly until 10 epochs, decays rapidly between 10 epochs and 130 epochs, and decays nearly linearly after 130 epochs, until it decays to 0 after 150 epochs, and the training of the inverse model is completed. We set up two control experiments for the 2D-resnet18 inverse model, including 1D-MLP, 1D-resnet18 model. The 1D fully connected network model has 8 layers; each layer contains 800 neurons; and the activation function uses the lrelu activation function. The remaining parameters of the 1D-MLP and 1D-resnet18 models are the same as those of the 2D-resnet18 model. The training losses as well as the test losses for the three inverse models are shown in Figs. 7(a) and (b). Among the three inverse models, although the 2D-resnet18 model has

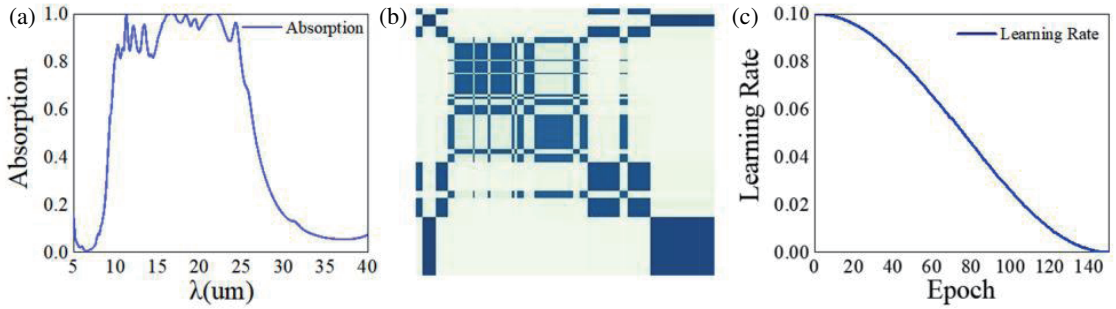

FIGURE 6. (a) One-dimensional spectral profile. (b) Two-dimensional image of the spectrum after MTF conversion. (c) 2D-resnet18 model learning rate decay curve.

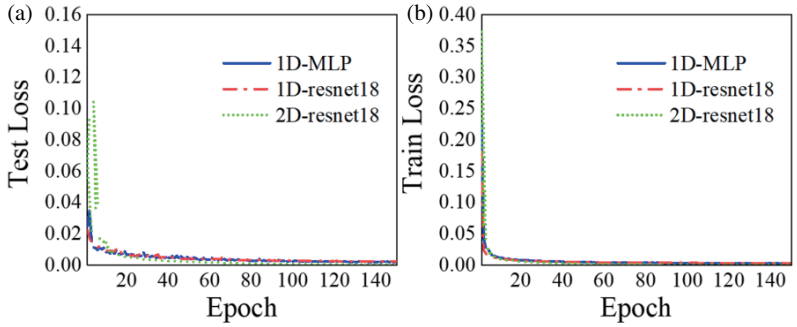

FIGURE 7. Comparison of (a) training loss as well as (b) testing loss for three inverse network models. The solid line is the fully connected network model with one-dimensional training data, the dotted line is the resnet18 network model with one-dimensional data, and the dotted line is the resnet18 network model with two-dimensional training data.

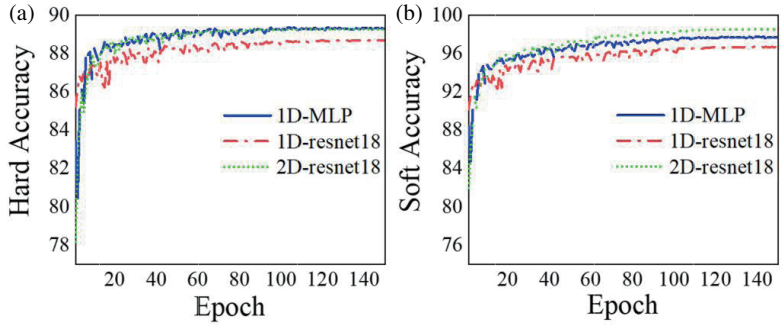

FIGURE 8. Three inverse models (a) hard accuracy curve as well as (b) soft accuracy curve. The solid line is the fully connected network model with one-dimensional training data, the dotted line is the resnet18 network model with one-dimensional data, and the dotted line is the resnet18 network model with two-dimensional training data.

the largest initial training loss and testing loss, its training loss as well as testing loss decreases at a fast rate. The training loss is smaller than that of the 1D-MLP model and the 1D-resnet18 model after 9 epochs. After 150 epochs, the training loss and test loss of the 2D-resnet18 model are the smallest among the three models, 0.0006 and 0.0004, respectively, so the training results of the 2D-resnet18 model are significantly better than the other two models.

We input the real structural parameters into the trained three models to obtain the three predicted structural parameters. These three predicted parameters are then input to the trained forward model together with the real structural parameters, and the corresponding spectra are obtained for comparison. The accuracy of the model is calculated. The accuracy of the model is calculated from the hard accuracy of the real spectra and the spectra of the predicted structural parameters obtained by the forward model, and the soft accuracy of the spectra of the real structural parameters and the predicted structural parameters obtained by the forward model.

$$hard\ accuracy = 1 - \frac{\sqrt{\sum_{i=1}^{n}(p_i - o_i)^2}}{\sqrt{\sum_{i=1}^{n} o_i^2}} \tag{15}$$

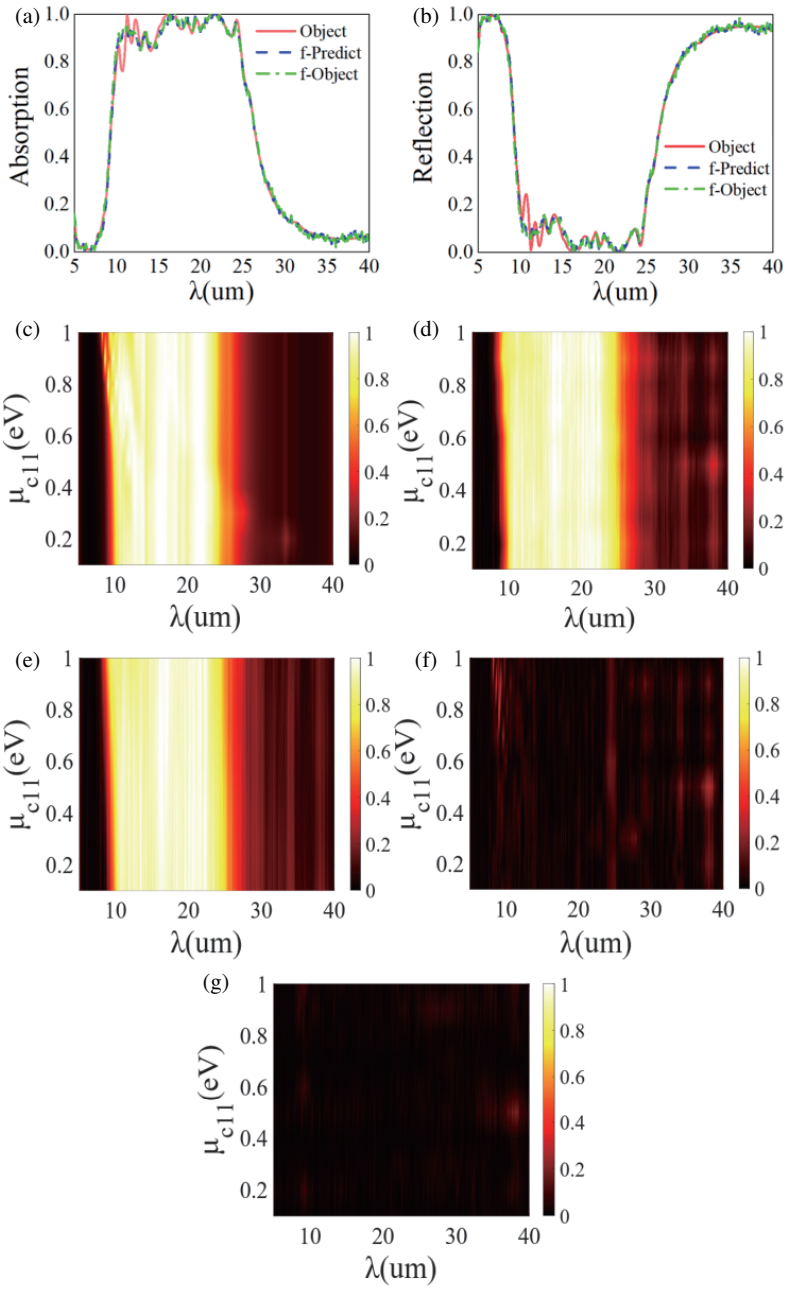

FIGURE 9. Comparison of the spectra obtained from the 2D-resnet18 model for the predicted structural parameters via the forward model with the true spectra and the spectral curves obtained from the true parameters via the forward model when $a_1 = 142\,\text{nm}$, $b_1 = 182\,\text{nm}$, $a_3 = 221\,\text{nm}$, $b_3 = 156\,\text{nm}$, $\mu_{c12} = 0.5\,\text{eV}$, $\mu_{c22} = 0.8\,\text{eV}$, $\mu_{c32} = 0.7\,\text{eV}$, $\mu_{c11} = 0.6\,\text{eV}$, $\mu_{c21} = 0.6\,\text{eV}$, $\mu_{c31} = 0.3\,\text{eV}$, (a) absorbance curve and (b) reflectance curve. $a_1 = 131\,\text{nm}$, $b_1 = 174\,\text{nm}$, $a_3 = 221\,\text{nm}$, $b_3 = 156\,\text{nm}$, $\mu_{c12} = 0.5\,\text{eV}$, $\mu_{c22} = 0.8\,\text{eV}$, $\mu_{c32} = 0.7\,\text{eV}$, $\mu_{c21} = 0.2\,\text{eV}$, $\mu_{c31} = 0.3\,\text{eV}$, and μ_{c11} varies from 0.1 eV to 1 eV, (c) thermogram of the real spectrum, (d) predicted spectrum of the heat map, (e) heat map of the spectrum obtained by the forward model for the real structural parameters, (f) heat map of the difference between the real spectrum and the predicted spectrum, (g) heat map of the difference between the spectrum obtained by the forward model for the real structural parameters and the predicted spectrum.

$$soft\ accuracy = 1 - \frac{\sqrt{\sum_{i=1}^{n}(p_i - o'_i)^2}}{\sqrt{\sum_{i=1}^{n} o'^2_i}} \tag{16}$$

where n denotes the sampling points of the spectra, p_i the spectra obtained by the forward model for the predicted structural parameters, o_i the real spectra obtained by the FEM method analysis for the real structural parameters, and o'_i the spectra obtained by the forward model for the real structural parameters.

Comparing the hard accuracy of the three models in Fig. 8(a), the 1D-MLP model and 2D-resnet18 model have similar final values of hard accuracy, which is approximately 89.3%; the

1D-resnet18 model has a worse result, 88.7%. However, as seen in Fig. 8(b), the final values of the hard accuracy of the 1D-MLP model and the 2D-resnet18 model are similar, but the final values of the soft accuracy of the two differ greatly by nearly 1%, with the final value of the soft accuracy of the 1D-MLP model being 97.6% and the final value of the 2D-resnet18 model being 98.5%. This is mainly because the forward model that we made is bottle-necked, and its accuracy has a threshold value, i.e., when the error between the predicted structural parameters and the real structural parameters is less than a certain value. No matter how small its error is, the accuracy of the model will not grow and maintain around a fixed value. Therefore, among the two accuracies, we should use soft accuracy as the main performance discriminant parameter. In order to observe more obviously the changes in the spectral curves in each, we draw the specific spectral curve pairs in the test set as shown in Figs. 9(a)–(b). Figs. 9(c)–(g) reflect the spectral thermograms for various cases obtained by controlling the other parameters constant and continuously varying μ_{c11}. We can see that the spectral difference between the real structural parameters and those predicted by the inverse model obtained by the forward model is small and almost zero. This also reflects the accuracy of our inverse model prediction from the other side.

4. CONCLUSION

In this work, we have developed an inverse deep neural network model framework for agent networks applied to small data sets. We use small models to ensure the accuracy of the network and also use the agent network to reduce the use of finite element analysis methods when evaluating the model, which can greatly reduce the computational time and save computational cost. Second, we incorporate the idea and method of converting 1D data to 2D data in the training process and compare it with the 1D MLP model and the 1D resnet18 model in this paper. Our proposed model is significantly better than the former two and can achieve smaller loss and higher accuracy. This method is useful for training other 3D complex structure models.

ACKNOWLEDGEMENT

This work was supported in part by the National Nature Science Foundation of China under Grant 62271001, 62101333, by the Anhui Provincial Natural Science Foundation under Grant 2022AH030014, by Program for Excellent Scientific and Innovation Research Team under Grant 2022AH010002.

REFERENCES

[1] Ashton, M., J. Paul, S. B. Sinnott, and R. G. Hennig, "Topology-scaling identification of layered solids and stable exfoliated 2D materials," *Physical Review Letters*, Vol. 118, No. 10, 106101, 2017.

[2] Liu, G., W. Jin, and N. Xu, "Two-dimensional-material membranes: A new family of high-performance separation membranes," *Angewandte Chemie International Edition*, Vol. 55, No. 43, 13 384–13 397, 2016.

[3] Cao, Y., V. Fatemi, S. Fang, K. Watanabe, T. Taniguchi, E. Kaxiras, and P. Jarillo-Herrero, "Unconventional superconductivity in magic-angle graphene superlattices," *Nature*, Vol. 556, No. 7699, 43–50, 2018.

[4] Roldan, R., A. Castellanos-Gomez, E. Cappelluti, and F. Guinea, "Strain engineering in semiconducting two-dimensional crystals," *Journal of Physics: Condensed Matter*, Vol. 27, No. 31, 313201, 2015.

[5] Burch, K. S., D. Mandrus, and J.-G. Park, "Magnetism in two-dimensional van der waals materials," *Nature*, Vol. 563, No. 7729, 47–52, 2018.

[6] Xie, Y., X. Liu, F. Li, J. Zhu, and N. Feng, "Ultra-wideband enhancement on mid-infrared fingerprint sensing for 2D materials and analytes of monolayers by a metagrating," *Nanophotonics*, Vol. 9, No. 9, 2927–2935, 2020.

[7] Schwierz, F., J. Pezoldt, and R. Granzner, "Two-dimensional materials and their prospects in transistor electronics," *Nanoscale*, Vol. 7, No. 18, 8261–8283, 2015.

[8] Novoselov, K. S., A. K. Geim, S. V. Morozov, D.-E. Jiang, Y. Zhang, S. V. Dubonos, I. V. Grigorieva, and A. A. Firsov, "Electric field effect in atomically thin carbon films," *Science*, Vol. 306, No. 5696, 666–669, 2004.

[9] Wang, Y., J. Mao, X. Meng, L. Yu, D. Deng, and X. Bao, "Catalysis with two-dimensional materials confining single atoms: concept, design, and applications," *Chemical Reviews*, Vol. 119, No. 3, 1806–1854, 2018.

[10] Bonaccorso, F., Z. Sun, T. Hasan, and A. C. Ferrari, "Graphene photonics and optoelectronics," *Nature Photonics*, Vol. 4, No. 9, 611–622, 2010.

[11] Liu, X., T. Galfsky, Z. Sun, F. Xia, E.-C. Lin, Y.-H. Lee, S. Kena-Cohen, and V. M. Menon, "Strong light-matter coupling in two-dimensional atomic crystals," *Nature Photonics*, Vol. 9, No. 1, 30–34, 2015.

[12] Ren, T. and L. Chen, "Slow light enabled high-modulation-depth graphene modulator with plasmonic metasurfaces," *Optics Letters*, Vol. 44, No. 22, 5446–5449, 2019.

[13] Zhang, T., Q. Liu, Y. Dan, S. Yu, X. Han, J. Dai, and K. Xu, "Machine learning and evolutionary algorithm studies of graphene metamaterials for optimized plasmon-induced transparency," *Optics Express*, Vol. 28, No. 13, 18 899–18 916, 2020.

[14] Rodrigo, D., O. Limaj, D. Janner, D. Etezadi, F. J. G. De Abajo, V. Pruneri, and H. Altug, "Mid-infrared plasmonic biosensing with graphene," *Science*, Vol. 349, No. 6244, 165–168, 2015.

[15] Mueller, T., F. Xia, and P. Avouris, "Graphene photodetectors for high-speed optical communications," *Nature Photonics*, Vol. 4, No. 5, 297–301, 2010.

[16] Hu, G., J. Kang, L. W. T. Ng, X. Zhu, R. C. T. Howe, C. G. Jones, M. C. Hersam, and T. Hasan, "Functional inks and printing of two-dimensional materials," *Chemical Society Reviews*, Vol. 47, No. 9, 3265–3300, 2018.

[17] Xiang, D., C. Han, J. Wu, S. Zhong, Y. Liu, J. Lin, X. A. Zhang, H. W. Ping, B. Ozyilmaz, A. H. Neto, A. T. Wee, and W. Chen, "Surface transfer doping induced effective modulation on ambipolar characteristics of few-layer black phosphorus," *Nature Communications*, Vol. 6, No. 1, 6485, 2015.

[18] Huang, M., M. Wang, C. Chen, Z. Ma, X. Li, J. Han, and Y. Wu, "Broadband black-phosphorus photodetectors with high responsivity," *Adv. Mater*, Vol. 28, No. 18, 3481–3485, 2016.

[19] Abbas, A. N., B. Liu, L. Chen, Y. Ma, S. Cong, N. Aroonyadet, M. Kopf, T. Nilges, and C. Zhou, "Black phosphorus gas sensors," *Acs Nano*, Vol. 9, No. 5, 5618–5624, 2015.

[20] Li, L., Y. Yu, G. J. Ye, Q. Ge, X. Ou, H. Wu, D. Feng, X. H. Chen, and Y. Zhang, "Black phosphorus field-effect transistors," *Nature Nanotechnology*, Vol. 9, No. 5, 372–377, 2014.

[21] Dai, J. and X. C. Zeng, "Bilayer phosphorene: Effect of stacking order on bandgap and its potential applications in thin-film solar cells," *The Journal of Physical Chemistry Letters*, Vol. 5, No. 7, 1289–1293, 2014.

[22] Qiao, J., X. Kong, Z.-X. Hu, F. Yang, and W. Ji, "High-mobility transport anisotropy and linear dichroism in few-layer black phosphorus," *Nature Communications*, Vol. 5, No. 1, 4475, 2014.

[23] Higashitarumizu, N., S. Z. Uddin, D. Weinberg, N. S. Azar, I. R. Rahman, V. Wang, K. B. Crozier, E. Rabani, and A. Javey, "Anomalous thickness dependence of photoluminescence quantum yield in black phosphorous," *Nature Nanotechnology*, Vol. 18, No. 5, 507–513, 2023.

[24] Torun, E., H. P. C. Miranda, A. Molina-Sanchez, and L. Wirtz, "Interlayer and intralayer excitons in MoS2/WS2 and MoSe2/WSe2 heterobilayers," *Physical Review B*, Vol. 97, No. 24, 245427, 2018.

[25] Altintas, O., E. Unal, O. Akgol, M. Karaaslan, F. Karadag, and C. Sabah, "Design of a wide band metasurface as a linear to circular polarization converter," *Modern Physics Letters B*, Vol. 31, No. 30, 1750274, 2017.

[26] Abdulkarim, Y. I., M. Xiao, H. N. Awl, F. F. Muhammadsharif, T. Lang, S. R. Saeed, F. O. Alkurt, M. Bakir, M. Karaaslan, and J. Dong, "Simulation and lithographic fabrication of a triple band terahertz metamaterial absorber coated on flexible polyethylene terephthalate substrate," *Optical Materials Express*, Vol. 12, No. 1, 338–359, 2022.

[27] Dincer, F., M. Karaaslan, S. Colak, E. Tetik, O. Akgol, O. Altintas, and C. Sabah, "Multi-band polarization independent cylindrical metamaterial absorber and sensor application," *Modern Physics Letters B*, Vol. 30, No. 08, 1650095, 2016.

[28] Alkurt, F. O., O. Altintas, A. Atci, M. Bakir, E. Unal, O. Akgol, K. Delihaciouglu, M. Karaaslan, and C. Sabah, "Antenna-based microwave absorber for imaging in the frequencies of 1.8, 2.45, and 5.8 GHz," *Optical Engineering*, Vol. 57, No. 11, 113 102–113 102, 2018.

[29] Valagiannopoulos, C. A., "Arbitrary currents on circular cylinder with inhomogeneous cladding and RCS optimization," *Journal of Electromagnetic Waves and Applications*, Vol. 21, No. 5, 665–680, 2007.

[30] Qiu, T., X. Shi, J. Wang, Y. Li, S. Qu, Q. Cheng, T. Cui, and S. Sui, "Deep learning: A rapid and efficient route to automatic metasurface design," *Advanced Science*, Vol. 6, No. 12, 1900128, 2019.

[31] Peurifoy, J., Y. Shen, L. Jing, Y. Yang, F. Cano-Renteria, B. G. DeLacy, J. D. Joannopoulos, M. Tegmark, and M. Soljačić, "Nanophotonic particle simulation and inverse design using artificial neural networks," *Science Advances*, Vol. 4, No. 6, eaar4206, 2018.

[32] Koziel, S. and M. Abdullah, "Machine-learning-powered em-based framework for efficient and reliable design of low scattering metasurfaces," *IEEE Transactions on Microwave Theory and Techniques*, Vol. 69, No. 4, 2028–2041, 2021.

[33] Rodriguez, J. A., A. I. Abdalla, B. Wang, B. Lou, S. Fan, and M. A. Cappelli, "Inverse design of plasma metamaterial devices for optical computing," *Physical Review Applied*, Vol. 16, No. 1, 014023, 2021.

[34] He, W., M. Tong, Z. Xu, Y. Hu, T. Jiang, *et al.*, "Ultrafast all-optical terahertz modulation based on an inverse-designed metasurface," *Photonics Research*, Vol. 9, No. 6, 1099–1108, 2021.

[35] Yuan, L., L. Wang, X.-S. Yang, H. Huang, and B.-Z. Wang, "An efficient artificial neural network model for inverse design of metasurfaces," *IEEE Antennas and Wireless Propagation Letters*, Vol. 20, No. 6, 1013–1017, 2021.

[36] Zhu, R., T. Qiu, J. Wang, S. Sui, C. Hao, T. Liu, Y. Li, M. Feng, A. Zhang, C.-W. Qiu, *et al.*, "Phase-to-pattern inverse design paradigm for fast realization of functional metasurfaces via transfer learning," *Nature Communications*, Vol. 12, No. 1, 2974, 2021.

[37] Tan, Q., C. Qian, and H. Chen, "Inverse-designed metamaterials for on-chip combinational optical logic circuit," *Progress In Electromagnetics Research*, Vol. 176, 55–65, 2023.

[38] Tan, Q., C. Qian, T. Cai, B. Zheng, and H. Chen, "Solving multivariable equations with tandem metamaterial kernels," *Progress In Electromagnetics Research*, Vol. 175, 139–147, 2022.

[39] Lee, I., C. Kim, K. Ju, G. Jun, and G. Yoon, "Implementation of particle swarm optimization for complete inverse design of multilayered optical filters," *Applied Optics*, Vol. 62, No. 34, 8994–9001, 2023.

[40] Sheverdin, A., F. Monticone, and C. Valagiannopoulos, "Photonic inverse design with neural networks: The case of invisibility in the visible," *Physical Review Applied*, Vol. 14, No. 2, 024054, 2020.

[41] Liu, Z., D. Zhu, L. Raju, and W. Cai, "Tackling photonic inverse design with machine learning," *Advanced Science*, Vol. 8, No. 5, 2002923, 2021.

[42] Cen, C., Z. Yi, G. Zhang, Y. Zhang, C. Liang, X. Chen, Y. Tang, X. Ye, Y. Yi, J. Wang, *et al.*, "Theoretical design of a triple-band perfect metamaterial absorber in the thz frequency range," *Results in Physics*, Vol. 14, 102463, 2019.

[43] Cai, Y., K.-D. Xu, N. Feng, R. Guo, H. Lin, and J. Zhu, "Anisotropic infrared plasmonic broadband absorber based on graphene-black phosphorus multilayers," *Optics Express*, Vol. 27, No. 3, 3101–3112, 2019.

[44] Sensale-Rodriguez, B., R. Yan, M. M. Kelly, T. Fang, K. Tahy, W. S. Hwang, D. Jena, L. Liu, and H. G. Xing, "Broadband graphene terahertz modulators enabled by intraband transitions," *Nature Communications*, Vol. 3, No. 1, 780, 2012.

[45] Low, T., R. Roldan, H. Wang, F. Xia, P. Avouris, L. M. Moreno, and F. Guinea, "Plasmons and screening in monolayer and multilayer black phosphorus," *Physical Review Letters*, Vol. 113, No. 10, 106802, 2014.

[46] Wang, Z. and T. Oates, "Encoding time series as images for visual inspection and classification using tiled convolutional neural networks," in *Workshops at The Twenty-Ninth Aaai Conference on Artificial Intelligence*, 2015.

[47] Mukaka, M. M., "A guide to appropriate use of correlation coefficient in medical research," *Malawi Medical Journal*, Vol. 24, No. 3, 69–71, 2012.

[48] Abdi, H., "The kendall rank correlation coefficient," *Mathematics*, 2006.

[49] He, K., X. Zhang, S. Ren, and J. Sun, "Deep residual learning for image recognition," in *Proceedings of The IEEE Conference on Computer Vision and Pattern Recognition*, 770–778, Las Vegas, NV, USA, 2016.